




# Strengthening mechanisms and high-temperature oxidation properties of laser-clad TaNbZrTi refractory high entropy alloy coatings

Jia-li Zhou<sup>1</sup>, Yan-hai Cheng<sup>1,\*</sup> , Hao Chen<sup>1</sup>, Kun Ma<sup>1</sup>, Yi-xing Wan<sup>1</sup>, and Jin-yong Yang<sup>1</sup>

<sup>1</sup> School of Mechanical and Electrical Engineering, China University of Mining and Technology, Xuzhou, People's Republic of China

**Received:** 31 July 2023

**Accepted:** 16 October 2023

**Published online:**  
8 November 2023

© The Author(s), under exclusive licence to Springer Science+Business Media, LLC, part of Springer Nature, 2023

## ABSTRACT

In the quest to enhance the performance of conventional high-temperature alloys, the limitations of existing materials have become apparent. Refractory high entropy alloys (RHEAs) have emerged as promising candidates, exhibiting exceptional high-temperature properties and offering a novel perspective on advanced materials for extreme environments. This study systematically determined optimal process parameters via single-channel laser cladding (LC), resulting in the development of multi-channel TaNbZrTi RHEA coatings. The investigation encompassed an in-depth analysis of microstructure and oxidation behavior across a temperature range spanning from 800 to 1200 °C. The findings elucidated the complex composition of the coating, characterized by the interplay of BCC1, BCC2, and Fe<sub>2</sub>Nb phases. The theoretical yield strength of the coating was calculated at 1816.1 MPa, with contributions from solution strengthening, precipitation strengthening, fine crystal strengthening, and alloy foundation strength, standing at 41.1%, 41.5%, 5.5%, and 11.9%, respectively. At 800, 1000 and 1200 °C, the oxide thickness of the coating is 1.4, 2.9, and 34.5 μm, respectively. The transition of BCC2 phase at elevated temperatures and the diffusion of Fe from the substrate emerged as pivotal factors contributing to catastrophic oxidation observed at 1200 °C. Importantly, the diffusion of substrate elements facilitated the formation of Fe<sub>2</sub>Nb phase, which exhibited robust precipitation strengthening effects, further enhancing the coating overall strength. However, the protective role of Fe oxides proved inadequate, leading to the vulnerability of the oxidation layer and its propensity to fracture, thereby compromising the high-temperature oxidation resistance of the coating.

Handling Editor: Catalin Croitoru.

Address correspondence to E-mail: chyh1007@cumt.edu.cn

## Introduction

As a groundbreaking concept in alloy design, high entropy alloys (HEAs) have demonstrated their potential applications across diverse sectors, including aerospace, medical instruments, national defense, nuclear energy engineering, and more [1, 2]. Among the remarkable HEAs, refractory high entropy alloys (RHEAs), composed of a versatile array of refractory metal elements, exhibit exceptional high-temperature resistance. They hold substantial promise for use as surface oxidation-resistant coatings for ultra-high-temperature components [3, 4]. However, RHEAs pose unique challenges due to their high melting points and brittleness at room temperature, making their preparation and forming quality inherently difficult [5, 6]. Various methods have been explored for the preparation of RHEAs coatings, including laser cladding (LC) [7], magnetron sputtering [8], electron beam cladding [9], vacuum arc deposition [10], and line arc additive manufacturing [11]. Among these methods, LC stands out due to its simplicity, high energy density, efficient cladding process, and excellent coating-substrate bonding, rendering it the most widely adopted approach for RHEA coatings [4, 12].

The high-temperature oxidation resistance of RHEA coatings has been extensively investigated in prior research. Di et al. [13] conducted a study on the oxidation behavior of  $\text{Ti}_{38}\text{V}_{15}\text{Nb}_{23}\text{Hf}_{24}$  RHEAs at 700–1300 °C. Below 1000 °C, a dense mixed oxide film was formed on the alloy surface, effectively hindering the diffusion of O. Above 1000 °C, decomposition of oxide film led to catastrophic oxidation. Yan et al. [14] reported the oxidation mechanism of WTaNbTiAl alloy at 1000 °C–12 h. The composite oxides formed at high temperature could effectively prevent O invasion and the diffusion of metal cation. Zhang et al. [15] found that the oxidation weight gain of NbZrTiCrAl RHEAs at 800 and 1000 °C was in line with parabolic oxidation kinetics, while at 1200 °C, the oxidation exhibited a linear pattern. Wang et al. [16] delved into adsorption energy of atoms and O in AlNbTiZr RHEAs based on first principles, and explained the oxidation mechanism of the alloy. Most of the alloy oxide layer was  $\text{Al}_2\text{O}_3$  because Al–O bond was stronger than Ti–O bond, but Ti would reduce the stability of  $\text{Al}_2\text{O}_3$ . Yurchenko et al. [17] obtained eutectic, subeutectic and hypereutectic RHEAs by adjusting the molar ratio of Al and Ti in AlCrNbTiZr RHEAs. They analyzed the mechanisms underlying

high-temperature oxidation failure and found that an increase in the Al/Ti ratio resulted in higher  $\text{Al}_2\text{O}_3$  content in the mixed oxide layer, reducing oxidation weight gain but increasing the susceptibility to oxide layer cracking.

The aforementioned studies have consistently demonstrated that RHEAs exhibit superior oxidation resistance compared to conventional alloys, owing to the delay diffusion effect [13, 18]. However, it is imperative to emphasize that the formation of a dense oxide layer is pivotal for ensuring the high-temperature oxidation resistance of these alloys. Typically, the oxide layer on RHEAs provides effective protection at temperatures below 1000 °C. Nevertheless, it is noteworthy that the occurrence of cracking or volatilization of the oxide layer beyond 1200 °C can result in catastrophic oxidation of the alloy [15, 19, 20]. While existing research predominantly centers on the oxidation resistance of as-cast RHEAs prepared through melting processes, there remains a noticeable gap in the investigation of RHEA coatings prepared using LC. Additionally, the influence of substrate element diffusion on the properties of these coatings is often overlooked.

The quest for enhancing the performance of conventional high-temperature alloys has reached its limits. Against this backdrop, the remarkable potential of RHEAs and their applications were explored, offering a fresh perspective on advanced materials for extreme environments. In this work, appropriate laser cladding process parameters were determined according to coating hardness and element composition, and TaNbZrTi RHEA coatings were prepared. The microstructure and element distribution of TaNbZrTi RHEA coatings were analyzed, and the strengthening mechanism was discussed. Furthermore, the oxidation behavior of the coatings at 800, 1000 and 1200 °C was tested, followed by a detailed analysis of the oxidation mechanisms.

## Experimental procedures

### Sample preparation

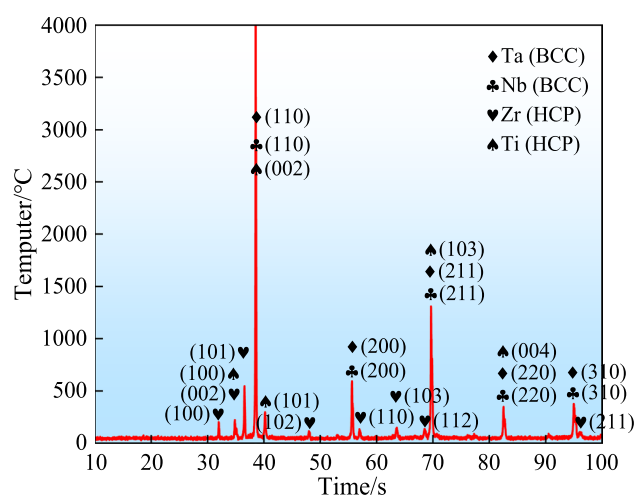
The substrate was 316 stainless steel tube with diameter of 60 mm, thickness of 5.5 mm and length of 900 mm. Its chemical composition is shown in Table 1. The powder is made of elemental Nb, Ta, Zr and Ti powder mixed by mechanical ball milling. The

**Table 1** Chemical element composition of 316 stainless steel

Elements	Ni	Cr	Mo	S	P	Mn	Si	C	Fe
Content/at%	11	18	1.5	0.05	0.06	2	2	0.37	Bal

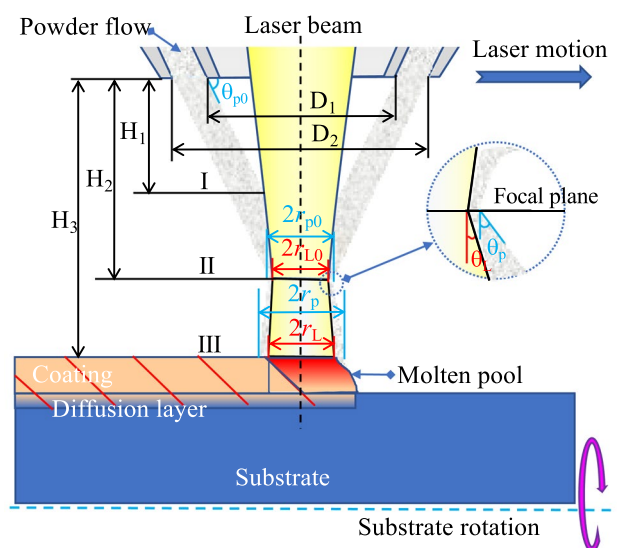
**Table 2** Specifications and thermophysical properties of cladding powders

Elements	Ta	Nb	Zr	Ti
Shape	Non-spherical	Spherical	Spherical	Spherical
Size/ $\mu\text{m}$	15–53	15–53	45–100	15–53
Melting point/ $^{\circ}\text{C}$	2996	2468	1852	1668
Boiling point/ $^{\circ}\text{C}$	5425	4742	4377	3260
Latent heat of fusion /kJ/mol	31.6	26.4	16.9	15.5
Latent heat of vaporization /kJ/mol	743	682	58.2	421

**Figure 1** XRD analysis of cladded powder.

specifications and thermal properties of the powder are listed in Table 2. The latent heat of vaporization of Zr powder is low. The size of 45–100  $\mu\text{m}$  was selected to avoid vaporization in LC. The size of other powders is 15–53  $\mu\text{m}$ . XQM-2A type planetary ball mill was used to mix powder. The grinding parameters were: speed of 400 rpm, ball-powder ratio of 3:1, time of 1.5 h, temperature of 25  $^{\circ}\text{C}$ . The XRD analysis of the mixed powder is shown in Fig. 1. The powder mixture consisted of Ta and Nb with BCC structure, as well as Zr and Ti with HCP structure. The powder was free of impurities and no phase transformation occurred during mixing.

The LC experiment utilized LYMR02-6000W type fiber laser equipment. Due to the significant difference in melting point between powder and substrate, high laser power is easy to cause serious element diffusion. Therefore, referring to the method of ultra-high speed

**Figure 2** Schematic diagram of laser-powder interaction in LC.

laser cladding, increasing the defocusing amount can make the laser energy more effective on the powder. The powder is melted before entering the molten pool and the thermal effect of the laser beam on the substrate is reduced. Figure 2 presents a schematic diagram of the laser-powder interaction during LC in this study.  $D_1$  and  $D_2$  are the inner and outer diameter of the powder feeding port.  $\theta_p$  and  $\theta_L$  are the divergence angle of the powder flow and laser beam, and  $\theta_{p0}$  is the incident angle of the powder flow.  $r_p$  and  $r_L$  are the powder spot and laser spot radius on the substrate,  $r_{p0}$  and  $r_{L0}$  are the powder spot and laser spot radius on the focal plane. The laser-powder interaction can be divided into three stages. Stage I: the powder converges from the outlet to the focal plane at the distance of  $H_1$ . Stage II: The powder enters the laser beam and

is heated continuously at the distance of  $H_2-H_1$ . Stage III: the powder is melted and forced into the molten pool by shielding gas and gravity at the distance of  $H_3-H_2$ .

In order to determine the appropriate process parameters of LC, the single-channel LC was used for pre-test, and four groups of process parameters were selected. Parameters: laser power was 2000, 2500, 2700 and 2900 W, scanning speed was 5 mm/s, spot diameter was 3 mm, defocus was +2 mm, powder delivery speed was 12 g/min, carrier gas flow rate was 12 L/min, shielding gas flow rate was 10 L/min. The appropriate laser power of 2500 W was determined by further analysis of the elemental composition and hardness of the coatings. According to the above parameters and 50% overlap rate, the multi-channel cladding layer was prepared to characterize the microstructure and high-temperature oxidation resistance.

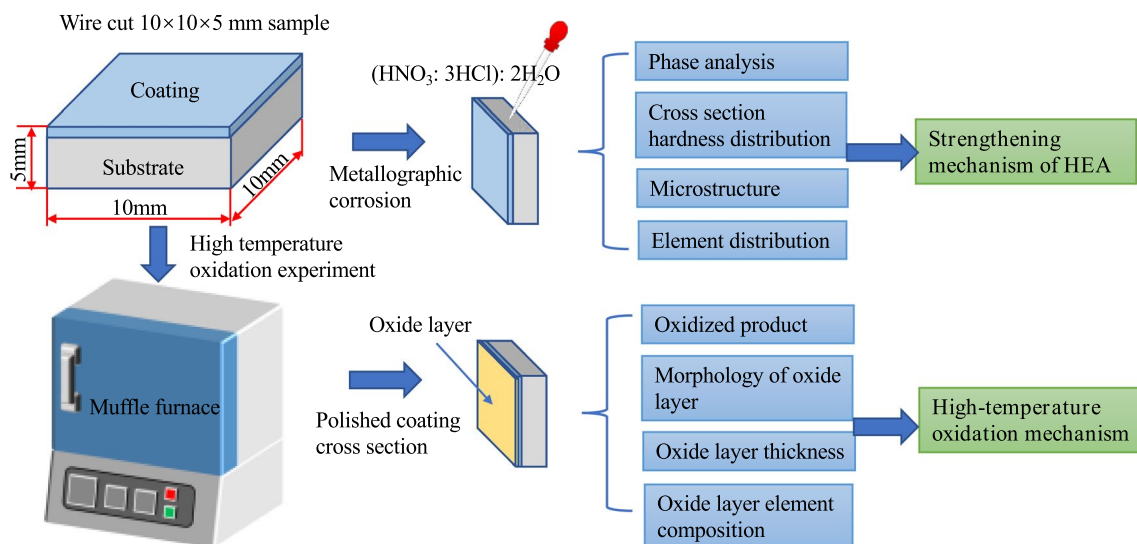
### Characterization methods

Figure 3 shows the flow of coating characterization and analysis. After LC, the cladding workpieces were cut into  $10 \times 10 \times 5$  mm sample blocks. The sample surfaces and cross-sections were mechanically polished with 80–2000# sandpapers, and were polished by diamond polishing agent with particle size of 0.5  $\mu\text{m}$ .

HVS-1000A type microhardness tester was utilized to measure the hardness distribution on the cross section of the coating. The average value of 3 points in

each depth plane test is the hardness of coatings. The load was 300 g and the load retention time was 10 s. Metallographic corrosion was carried out on the section of the sample, the caustic agent was dilute aqua regia ( $(\text{HNO}_3: 3\text{HCl}): 2\text{H}_2\text{O}$ ) (Tianjin Damao Chemical Reagent Factory), the time was 20 s. The micromorphology of the samples was observed by MAIA3 LMH type mode field emission scanning electron microscope (FSEM), and the element composition and distribution of the samples were analyzed by energy dispersion spectrometer (EDS). The phase composition of both the powder and the coating was analyzed using a D8 ADVANCE type X-ray diffractometer (XRD) with  $\text{Cu-K}\alpha$  radiation ( $\lambda = 1.5406 \text{ \AA}$ ). The identification of phases was conducted using Jade 6 software with the Level-1 PDF XRD database.

The high-temperature oxidation experiments were conducted using an AS2L-17 type muffle furnace. The oxidation duration was set to 1 h, with a heating rate of  $10 \text{ }^\circ\text{C}/\text{min}$ . Three different temperatures, namely 800, 1000, and  $1200 \text{ }^\circ\text{C}$ , were employed for the experiments. The experiments were carried out in an air atmosphere. The furnace temperature was gradually raised to the specified test temperature, and the sample block was subsequently introduced. Post-experiment, the sample block was allowed to cool within the furnace. For analysis of the oxidation mechanism, XRD, FSEM, and EDS were applied. The cross-sections of the coatings were mechanically lapped and polished. FSEM and EDS mapping were employed to



**Figure 3** Sample characterization and analysis flow chart.

characterize the oxide thickness and oxygen diffusion within the coatings. These analyses collectively aim to reveal key insights into the oxidation mechanism of TaNbZrTi RHEA coatings under high-temperature conditions.

## Results and analysis

### Laser power selection

In order to select the appropriate laser power, EDS analysis was performed on the 2000, 2500, 2700 and 2900 W single-channel coating surfaces, as shown in Fig. 4. The analysis revealed significant variations in the contents of Fe and Cr within the TaNbZrTi RHEA coatings as the laser power increased. The high dilution rate resulting from the high energy density had a pronounced impact on both coating composition and properties [21]. In the case of the 2000 W coating, the low content of Ta and Nb indicated that the laser power was insufficient, leading to only partial melting of high-melting-point Ta and Nb particles. Conversely, the coatings produced at 2700 and 2900 W exhibited low contents of Ti and Zr, suggesting that these coatings had been subjected to over-burning, resulting in the vaporization of some Zr and Ti. Additionally, the observation of a severe “splash” phenomenon during LC confirmed that the laser power was excessively high. This phenomenon was characterized by

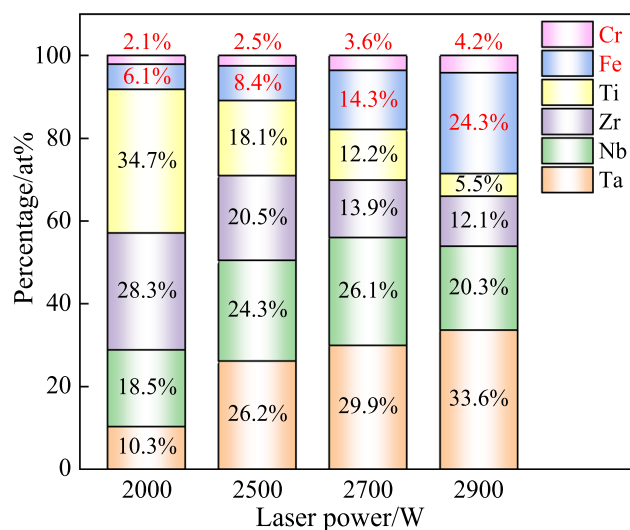


**Figure 4** EDS analysis of single-channel coating surface with different power.

a low-pressure area near the rapidly moving metal vapor, which induced the surrounding Ar gas to infiltrate the molten pool, leading to reverse splashing. When the recoiling air force surpassed the gravitational force acting on metal particles and the tractive force of the shielding gas, the molten pool experienced splashing [22]. The reverse splashing, driven by the rapid evaporation of the metal solution, caused the ejection of metal droplets containing Ti and Zr with low melting points, as well as micro-molten powder particles composed of Ta and Nb with high melting points. Among these coatings, the composition of the coating prepared at 2500 W closely aligned with expectations, making it the most suitable choice for intended application.

Figure 5 shows the microhardness distribution of 2000, 2500, 2700 and 2900 W single-channel coating cross-sections. The corresponding average hardness of the coating and the substrate was  $433 \pm 16$ ,  $631 \pm 24$ ,  $511 \pm 23$ ,  $515 \pm 21$ , and  $181 \pm 7$  HV<sub>0.3</sub>, respectively. The primary strengthening mechanism observed in TaNbZrTi RHEAs is solution strengthening. The random arrangement of Ta, Nb, Zr, and Ti elements in equal molar ratios forms a BCC solid solution [23]. Variations in atomic properties lead to lattice distortions, making the material more resistant to dislocation slip, resulting in enhanced strength [24]. However, all coatings produced using different laser power settings contained impurity elements, leading to significant variations in coating composition. Impurity elements

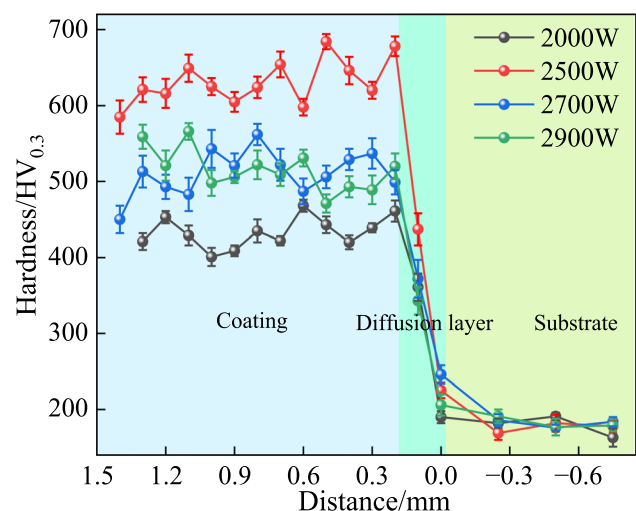


**Figure 5** Microhardness distribution of single-channel coating cross-section with different power.

can disrupt the ideal lattice structure and introduce defects, thereby diminishing the effectiveness of solution strengthening. The composition achieved with a 2500 W laser power setting was the closest to the expected composition and exhibited the highest hardness. Consequently, 2500 W laser power was selected to prepare multi-channel coating.

## Microstructure analysis

### XRD analysis of coating

Figure 6 displays XRD pattern of the multi-channel TaNbZrTi coating surface. The coating was composed of the main phase BCC1, the secondary phase BCC2, and the intermetallic compound  $\text{Fe}_2\text{Nb}$ . BCC1 + BCC2 phase represents the TaNbZrTi RHEAs phase structure. In this structure, Fe from the substrate diffused into the coating and combined with Nb to form  $\text{Fe}_2\text{Nb}$  (PDF #17-0908). Notably, due to the low concentration of Cr, a corresponding diffraction peak for Cr was not observed.

### Microscopic morphology

Figure 7a–d illustrate the microscopic morphologies of various cross-sections of the TaNbZrTi coating, including the top, middle, bottom, and lap areas. The top section of the coating predominantly featured fine cellular crystals, while the middle section exhibited coarser dendritic structures, and the lap area displayed strip-like grains. These variations in grain

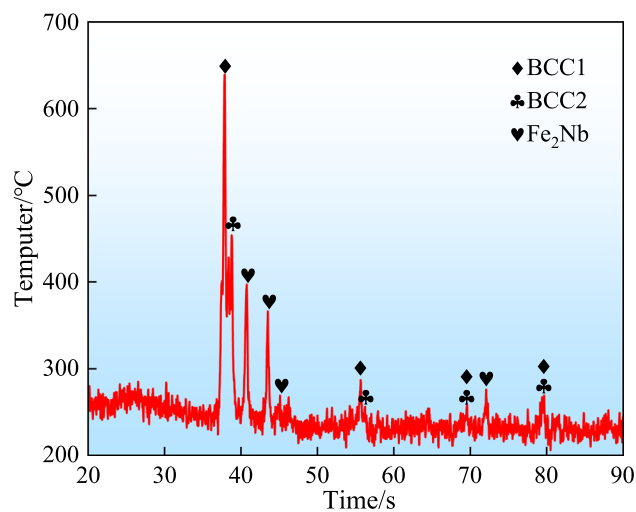


**Figure 6** XRD analysis of multi-channel coating surface.

morphology within the coating can be explained by considering the non-equilibrium solidification characteristics inherent to LC [6]. The significant difference in grain size between the top section and the middle as well as bottom sections could be attributed to the high cooling rate experienced by the molten pool surface during the LC process. To measure the average crystal size, a cutting line method was employed, revealing an average size of  $5.71 \mu\text{m}$  in Fig. 7a. Quantifying the grain size of the dendrites in the middle and bottom sections was challenging due to their irregular secondary dendrite arms.

Additionally, the coating exhibited distinct primary phase BCC1 (bright regions) and secondary phase BCC2 (dark regions). To quantify the area of the BCC1 phase, the gray threshold module in Image-J software was utilized, as depicted in Fig. 7e. The ratio of BCC1 phase content at various locations within the coating was as follows: 77.2% at the top, 75.8% at the middle, 72.7% at the bottom, and 75.5% at the lap area. The higher content of the BCC1 phase at the top of the coating can be attributed to the compact arrangement of fine cellular crystals and the presence of small intergranular gaps. This specific microstructure contributes to improved mechanical properties and enhanced structural integrity within the coating.

### Element distribution

To gain further insights into the microstructure of the TaNbZrTi coating and to elucidate the solidification characteristics of the molten pool, EDS mapping analysis was conducted on various regions of coatings. Figure 8 illustrates the results of the EDS analysis within the cellular crystal region. In the EDS mapping, Ta and Nb were found to be enriched within the BCC1 phase, whereas Zr and Ti exhibited higher concentrations within the BCC2 phase, as depicted in Fig. 8c. During the solidification process of the molten pool, elements with high melting points, such as Ta ( $2996 \text{ }^\circ\text{C}$ ) and Nb ( $2468 \text{ }^\circ\text{C}$ ), were preferentially precipitated. These high-melting-point elements combined with other alloy constituents to form a BCC simple solid solution, rich in Ta and Nb [25]. In contrast, elements with lower melting points, namely Zr ( $1852 \text{ }^\circ\text{C}$ ) and Ti ( $1668 \text{ }^\circ\text{C}$ ), were present in higher quantities in the liquid phase. They filled the interstitial spaces within the primary BCC1 phase, resulting in the formation of the secondary phase BCC2, which was rich in Zr

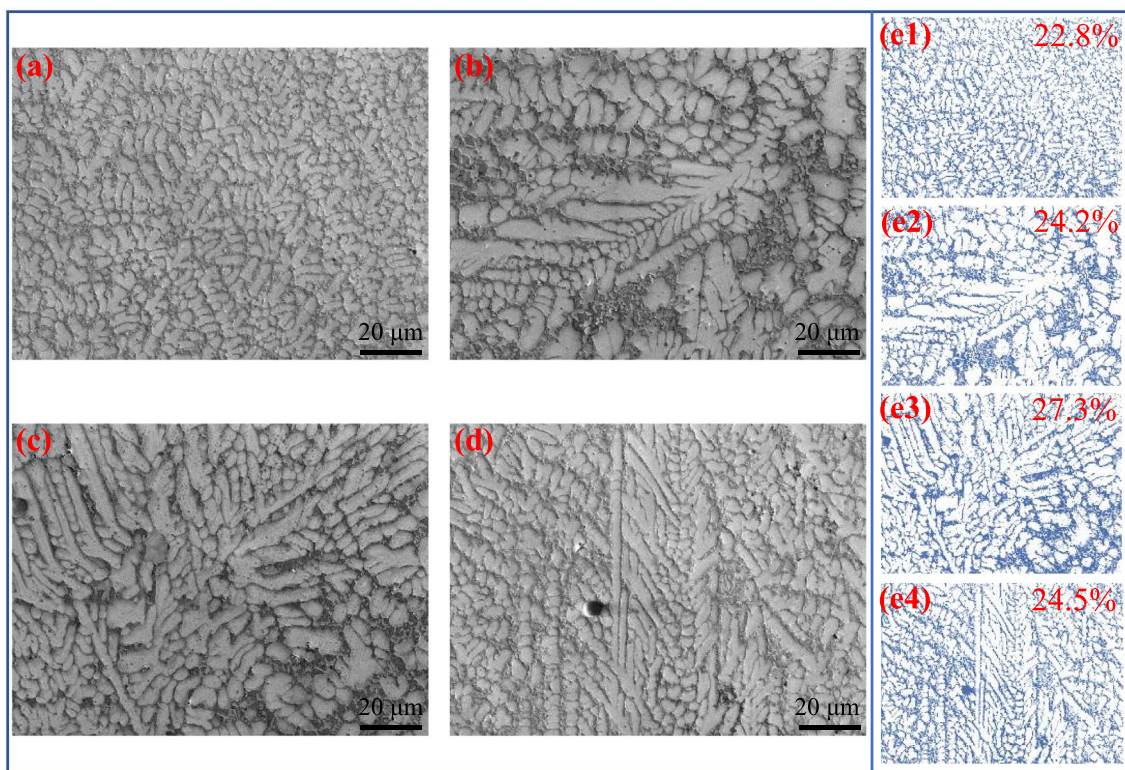


**Figure 7** Microstructure of TaNbZrTi coating: **a** Microstructure of coating at the top; **b** Microstructure of the coating at the middle; **c** Microstructure of the coating at the bottom; **d** Microstruc-

ture of the coating lap; **e1–e4** respectively correspond to the distribution of BCC1 phases (bright area) in (a)–(d).

and Ti. Figure 8b provides an overview of the element content within the cellular crystal region. Notably, when compared to the 2500 W single-channel coating, the multi-channel coating exhibited a significant reduction in the contents of impurity elements, such as Fe and Cr, as evidenced in Fig. 4. This reduction in impurity elements can be attributed to the fact that during multi-cladding, a portion of the laser energy was utilized to re-melt the preceding coating. Consequently, the actual dilution rate of the multi-channel coating was lower than that of the single cladding process [6]. Figure 8a reveals the presence of small particles with a diameter of 0.3  $\mu\text{m}$  scattered within the grains. EDS analysis confirmed these particles to be  $\text{Fe}_2\text{Nb}$  phases, as indicated in Table 3. Notably, the shear modulus of  $\text{Fe}_2\text{Nb}$  phase significantly exceeded that of the TaNbZrTi solid solution. The presence of these  $\text{Fe}_2\text{Nb}$  phases contributed to dispersion strengthening, thereby enhancing the overall hardness of the coating. This phenomenon was one of the key factors behind the higher hardness observed in the coating

in this study when compared to the as-cast TaNbZrTi RHEAs mentioned in the reference [26].

There were several un-melted particles with a radius of approximately 15  $\mu\text{m}$  in the coating, as illustrated in Fig. 9a. Heterogeneous nucleation also occurred on the surfaces of these un-melted particles, providing evidence that these particles remained un-melted within the molten pool rather than precipitating during the solidification process [27]. Further analysis using EDS confirmed that these particles were composed of un-melted Ta, as depicted in Fig. 9b, c. These un-melted Ta particles had a significant impact on the microstructure of the adjacent coatings. The presence of un-melted Ta particles resulted in a reduction in the Ta content within the molten metal liquid phase. This reduction, in turn, led to a decrease in the content of the BCC1 phase (bright region). Notably, Nb was substantially enriched in the heterogeneous nucleation sites that were adjacent to the un-melted Ta particles, while the Ta content remained relatively low. Additionally, the relative concentrations of Zr and Ti in the molten metal liquid phase increased. Zr became

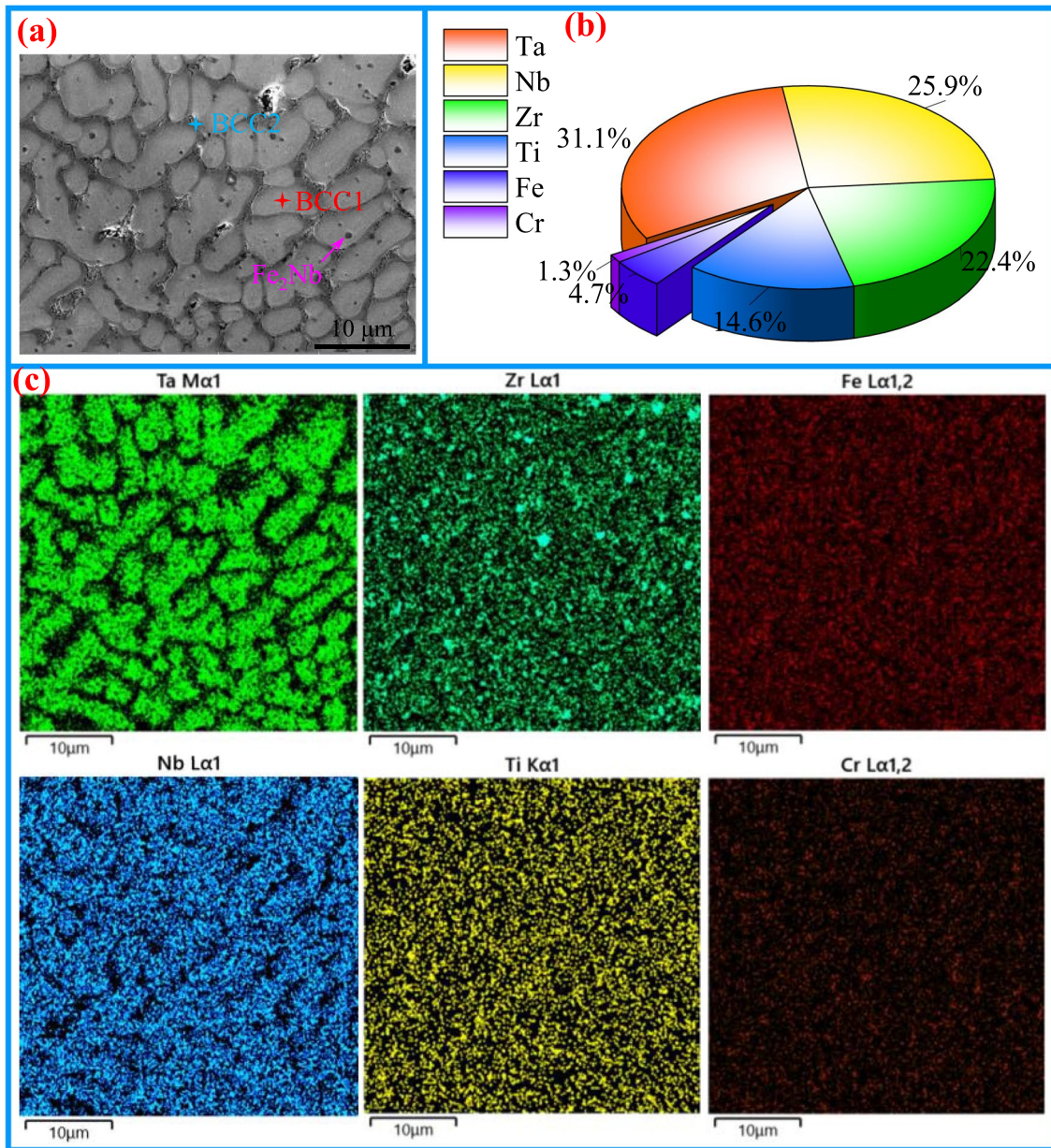


**Figure 8** EDS analysis of the cellular crystal: **a** Scanning position of EDS plane; **b** Element content statistics; **c** EDS mapping.

**Table 3** Components of BCC1, BCC2 and Fe<sub>2</sub>Nb (at%)

Elements	Ta	Nb	Zr	Ti	Fe	Cr
BCC1	47.2	27.1	10	12.7	2.7	0.3
BCC2	8.1	14.2	39.6	31.3	5.2	1.6
Fe <sub>2</sub> Nb point	10.5	32.1	3.6	2.5	51.3	–

predominantly isolated within the BCC1 phase, and the content of the BCC2 phase increased. Overall, the presence of un-melted Ta particles disrupted the

anticipated composition of the nearby coating, thereby having a detrimental effect on the coating structural integrity and intergranular fluidity.



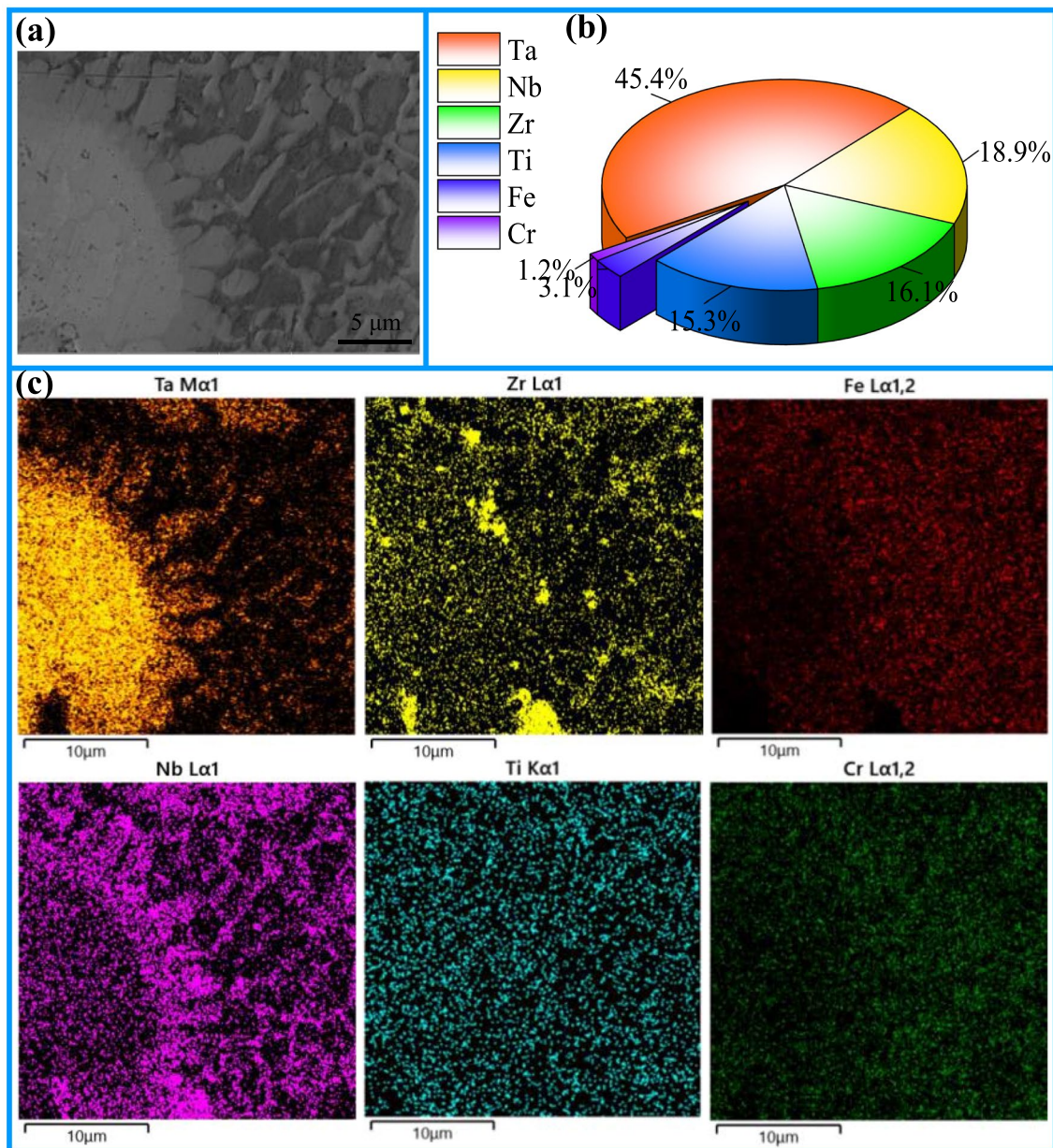


**Figure 9** EDS analysis of un-melted Ta particles: **a** Scanning position of EDS plane; **b** Element content statistics; **c** EDS mapping.

Figure 10 presents EDS analysis of the dendrite region within the coating. The elemental distribution within the dendritic structure exhibited similarities to that observed in the cellular crystals. Notably, there was a prominent enrichment of Ta within the dendritic crystal, with limited distribution of Nb extending beyond the crystal boundaries. Within the dendrites, the secondary dendrite arm spacing was relatively large, and this led to significant

enrichment of Zr outside the crystal boundaries. The distribution of Ti was less pronounced in this region. It is worth highlighting that impurity elements such as Fe and Cr were evenly distributed throughout the dendritic region, and their concentrations were elevated. This phenomenon could be attributed to the more conspicuous diffusion of elements from the substrate occurring in the central region of the molten pool.

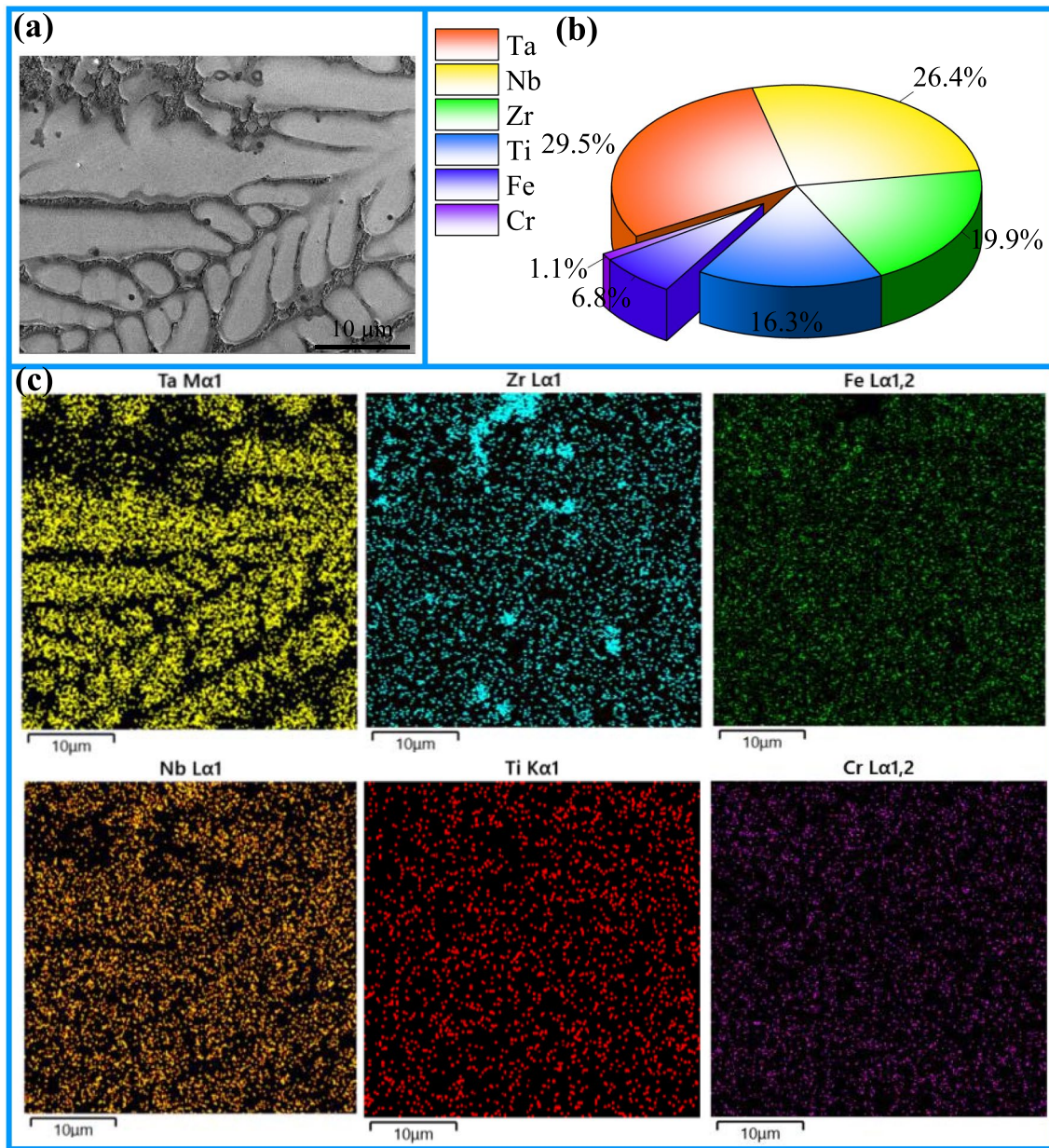


**Figure 10** EDS analysis of the dendrite region: **a** Scanning position of EDS plane; **b** Element content statistics; **c** EDS mapping.

## High temperature oxidation resistance

### *XRD analysis of oxide layer*

Figure 11 presents the XRD analysis of the TaNbZrTi coating surface following oxidation experiments conducted at 800, 1000, and 1200 °C. Prior to oxidation, the TaNbZrTi coating exhibited a BCC1 + BCC2 + Fe<sub>2</sub>Nb structure. However, the high-temperature oxidation led to the formation of distinct oxide products,

primarily consisting of Fe<sub>2</sub>O<sub>3</sub> (PDF #33-0664), TiO<sub>2</sub> (PDF #79-1640), and Nb<sub>2</sub>O<sub>5</sub> (PDF #19-0864). In the case of the 800 °C oxidation coating, the oxide layer observed was relatively thin. The XRD analysis of this coating revealed the presence of BCC1, BCC2, and Fe<sub>2</sub>Nb phases. Notably, the intensity of the oxide diffraction peak was relatively low in this instance. Conversely, the surfaces of the 1000 and 1200 °C oxidation coatings were noticeably covered with oxide layers. This suggests that the oxidation process became more

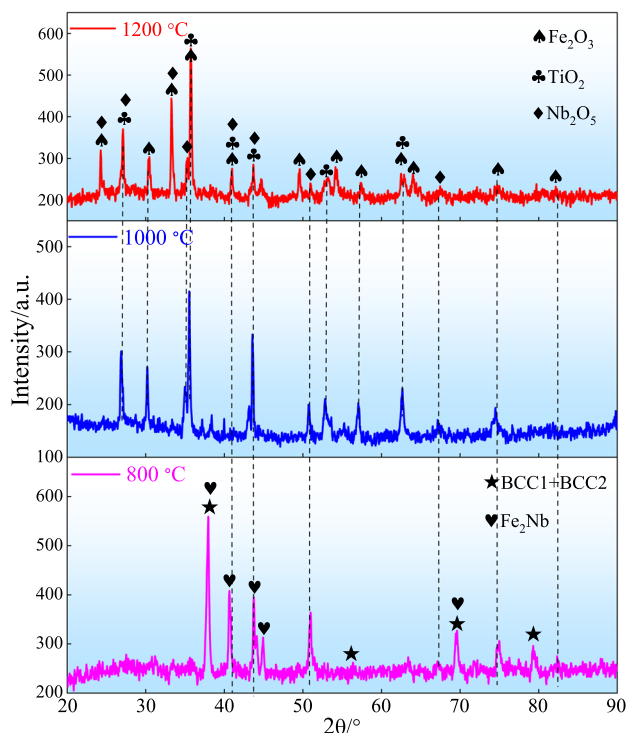


**Figure 11** XRD analysis of TaNbZrTi coating surface for oxidation experiments at 800, 1000 and 1200 °C.

pronounced at higher temperatures, resulting in a thicker and more extensive oxide layer formation on the coating surface.

#### *Oxidation morphology of coating surfaces*

Figure 12 depicts the oxide morphology and EDS analysis of the TaNbZrTi coating surface following high-temperature oxidation. At 800 °C, some granular oxides accumulated on the coating surface. The surface of BCC1 phase appeared relatively flat, while the BCC2 phase surface exhibited an evident lamellar oxide layer, as illustrated in Fig. 12a. Upon closer inspection in the enlarged image, Fig. 12d reveals cracking of the oxide layer on the BCC2 surface. EDS mapping of the 800 °C coating surface is presented in Fig. 12g. The BCC1 surfaces exhibited a low oxygen content, whereas the BCC2 surfaces were covered by oxides, primarily composed of  $\text{TiO}_2$ ,  $\text{Fe}_2\text{O}_3$ , and trace amounts of  $\text{Nb}_2\text{O}_5$ . In contrast, the surfaces of the 1000 °C and 1200 °C coatings were fully covered with oxides, as shown in Fig. 12b, c. Upon magnification, the oxide layer of the 1000 °C coating was seen to be

lamellar, while that of the 1200 °C coating was granular, as displayed in Fig. 12e, f. The granular oxide layer was no longer effective in preventing oxygen diffusion into the interior of the coating, leading to catastrophic oxidation of the coating [28, 29].

#### *Oxygen diffusion analysis of coating cross-sections*

In high-temperature oxidation experiments, changes in mass due to substrate oxidation inevitably impact the reliability of the coating weight gain curve. Therefore, the oxidation behavior of TaNbZrTi RHEAs at different temperatures was quantitatively characterized using the oxidation depth of the coating cross-section and the distribution of O. Figure 13 illustrates the oxide morphology and EDS analysis of TaNbZrTi coating cross-sections after exposure to high temperatures. At temperatures of 800, 1000, and 1200 °C, the oxide thickness of the coatings measured 1.4, 2.9, and 34.5  $\mu\text{m}$ , respectively. At 800 °C, the oxide layer appeared dense and tightly bonded to the coating, providing excellent protection. However, at 1000 °C, the oxide layer thickness increased, and while it remained relatively dense, the emergence of cracks at the interface between the oxide layer and the coating suggested a risk of cracking and potential spalling [30]. Notably, at 1200 °C, the oxide layer exhibited numerous cracks and pores. It had lost its ability to hinder O diffusion, leading to severe internal oxidation of the coating [29]. Internal oxidation not only accelerates the oxidation process within the coating but also increases the risk of surface peeling.

In the O distribution diagram, it was observed that O distribution below the oxide layer originated from airborne oxygen, while another part resulted from the diffusion of external oxygen into the coating in the high-temperature environment [31]. Furthermore, it was evident that the O content in the BCC2 phase was higher than that in the BCC1 phase. This phenomenon was particularly pronounced in the O distribution diagram of the oxidized coating at 1000 and 1200 °C, as depicted in Fig. 13b, c. At 1200 °C, the protective oxide films, such as  $\text{TiO}_2$  and  $\text{Cr}_2\text{O}_3$ , experienced deterioration, leading to increased O atom diffusion rates within the coating and ultimately resulting in catastrophic oxidation [29, 32].

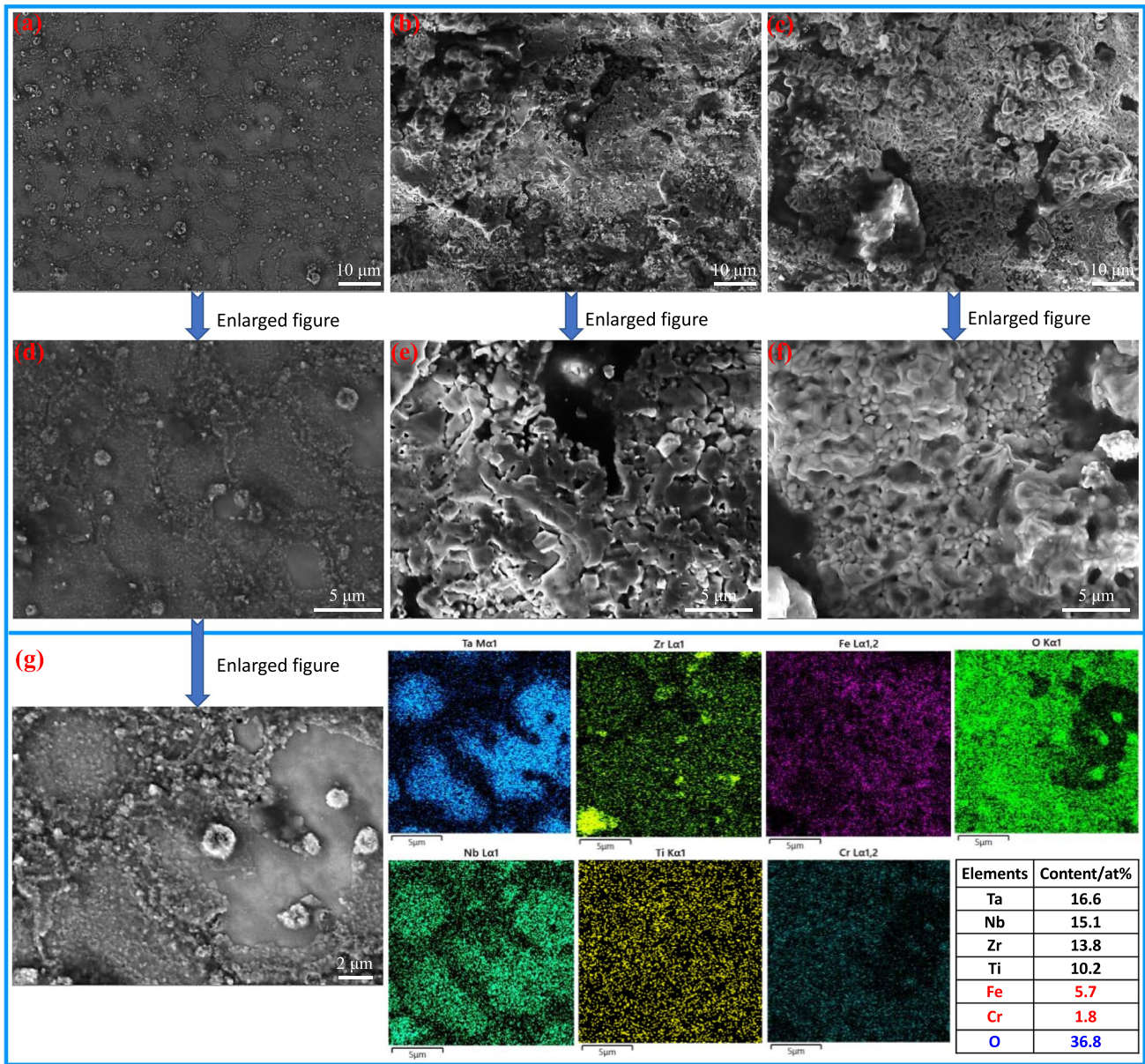


**Figure 12** Surface morphologies and EDS analysis of TaNbZrTi coatings at 800, 1000 and 1200 °C: **a**, **b** and **c** surface morphologies of TaNbZrTi coatings at 800, 1000 and 1200 °C, respec-

tively; **d**, **e** and **f** are the enlarged images of the corresponding oxide layer; **g** EDS mapping of the TaNbZrTi coating surface oxidized at 800 °C.

## Discussion

### Strengthening mechanism

Based on the experimental results presented above, it is evident that the diffusion of substrate elements significantly altered the coating properties compared with the literature. However, it is important to note

that the formation of a metallurgical bond between the coating and the substrate during LC inherently leads to the diffusion of substrate elements. As a result, it is essential to analyze the strengthening mechanism of HEAs.

Firstly, the mixing entropy ( $\Delta S_{mix}$ ), mixing enthalpy ( $\Delta H_{mix}$ ), atomic size difference ( $\delta$ ) and average valence electron concentration (VEC) of alloys were calculated, the formula for [6]:

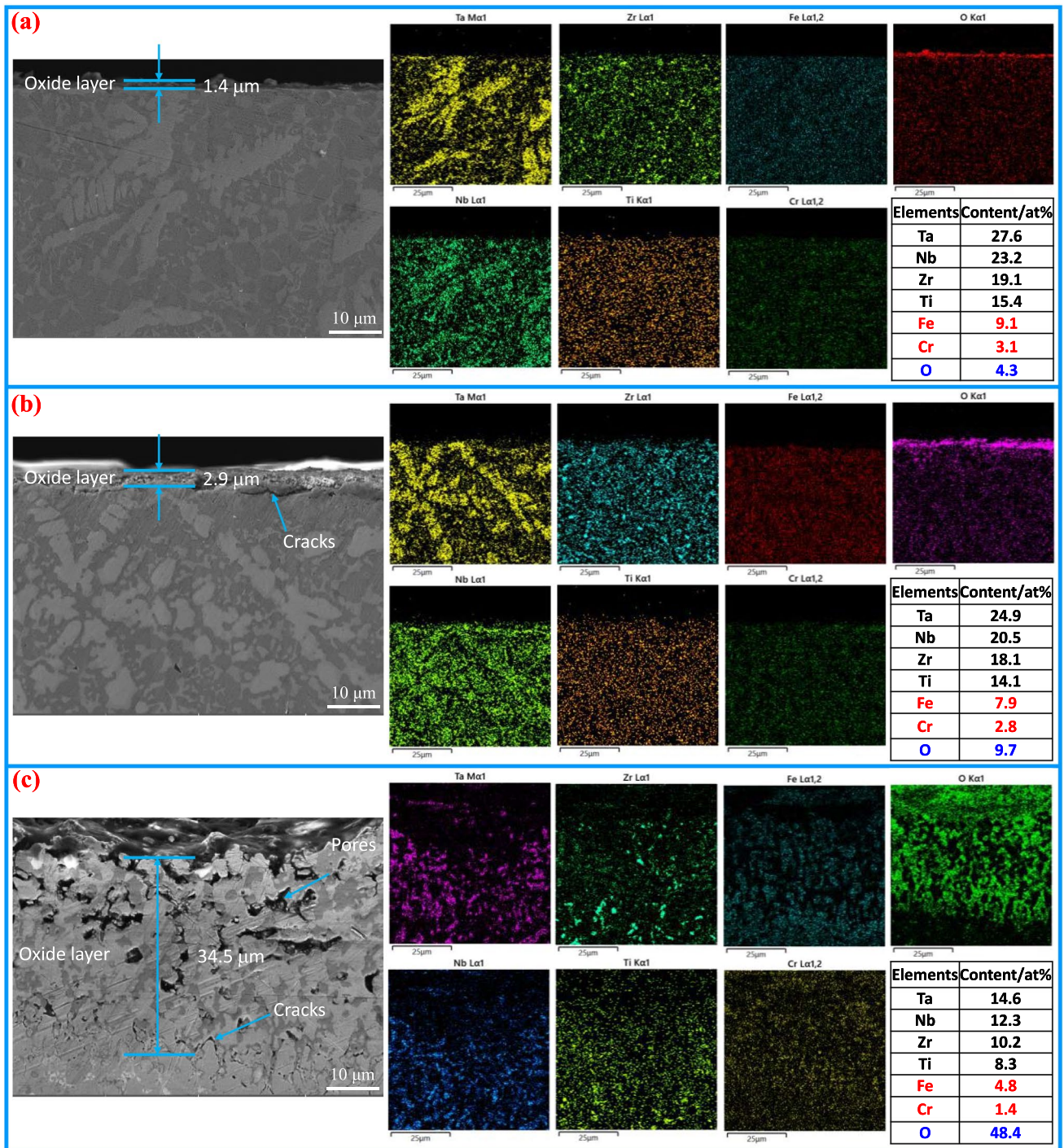


**Figure 13** Morphologies and EDS analysis of TaNbZrTi coating cross-sections at 800, 1000 and 1200 °C for high temperature oxidation experiments: **a** High temperature oxidation layer at

800 °C; **b** High temperature oxidation layer at 1000 °C; **c** High temperature oxidation layer at 1200 °C.

$$\Delta S_{\text{mix}} = -R \sum_{i=1}^n c_i \ln c_i \tag{1}$$

$$\Delta H_{\text{mix}} = \sum_{\substack{i=1 \\ i \neq j}}^n 4H_{AB}c_i c_j \tag{2}$$

$$\delta = \sqrt{\sum_{i=1}^n c_i \left(1 - \frac{r_i}{\bar{r}}\right)^2} \tag{3}$$

$$\text{VEC} = \sum_{i=1}^n c_i(\text{VEC})_i \tag{4}$$

where  $R$  is the gas constant;  $c_i$  is the mole fraction of the  $i$ -th element;  $c_j$  is the mole fraction of the  $j$ -th element and  $i \neq j$ ;  $H_{AB}$  is the mixing enthalpy between A element and B element; and  $r_i$  is the radius of the  $i$ -th atom;  $\bar{r}$  is the molar average atomic radius,  $\bar{r} = \sum_{i=1}^n c_i r_i$ .

Table 4 displays the property parameters for coating elements,  $T_m$  is the melting point of elements. Table 5 presents results obtained using Eqs. (1)–(4). Among these, A-HEA, the TaNbZrTi alloy with impurities, exhibited larger values for  $\Delta S_{\text{mix}}$ ,  $\delta$ , VEC and  $T_m$  when compared to the theoretical TaNbZrTi alloy (T-HEA) lacking impurities and featuring equimolar element ratios. Furthermore, the presence of impurities, specifically Fe and Cr in the coating, led to a transition from positive to negative  $\Delta H_{\text{mix}}$ . These findings suggest that impurity atoms enhanced both the high entropy and lattice distortion effects in the coating, increasing the propensity for intermetallic compound formation. Consequently, A-HEA formed the Fe<sub>2</sub>Nb phase and exhibited higher hardness. Additionally, BCC2 demonstrated a greater  $\delta$  than BCC1, indicating

**Table 5** Thermodynamic parameters of theoretical TaNbZrTi alloy (T-HEA) and actual TaNbZrTi alloy (A-HEA) containing impurities, BCC1 phase and BCC2 phase

Properties	$\Delta S_{\text{min}}/\text{J}/(\text{mol K})$	$\Delta H_{\text{min}}/\text{kJ}/\text{mol}$	$\delta/\%$	VEC	$T_m/\text{K}$
T-HEA	11.53	2.5	4.75	4.5	2527
A-HEA	12.72	−1.28	6.03	4.78	2612
BCC1	10.93	−0.3	4.29	4.86	2815
BCC2	11.89	−2.57	6.71	4.46	2240

more pronounced lattice distortion [24]. Furthermore,  $T_m$  of BCC1 exceeded that of BCC2, signifying superior high-temperature performance.

The theoretical yield strength of the alloy ( $\sigma_y$ ) can be represented as:

$$\sigma_y \approx (\sigma_{0.2})_{\text{mix}} + \Delta\sigma \tag{5}$$

where  $(\sigma_{0.2})_{\text{mix}}$  is the base strength estimated from the yield strength of pure metals using the mixing rule.

$$(\sigma_{0.2})_{\text{mix}} = \sum c_i \sigma_{0.2(i)} \tag{6}$$

where  $\sigma_{0.2(i)}$  is the yield strength of pure metal.

$\Delta\sigma$  takes into account grain boundary strengthening  $\sigma_{gb}$ , solid solution strengthening  $\sigma_s$ , precipitation strengthening  $\sigma_p$  and dislocation strengthening  $\sigma_d$ :

$$\Delta\sigma = \sigma_g + \sigma_s + \sigma_p + \sigma_d \tag{7}$$

For BCC structure RHEAs, the contribution of dislocation strengthening to alloy strength is negligible [33]. Among them, grain boundary strengthening is expressed as:

$$\sigma_g = kd^{-\frac{1}{2}} \tag{8}$$

where  $k$  is constant,  $k = 240 \text{ MPa } \mu\text{m}^{1/2}$ , from HfNbTaTiZr [34];  $d$  is the average grain size;  $\sigma_g = 100.4 \text{ MPa}$ .

**Table 4** Property parameters of coating elements

Element	$\Delta H_{\text{mix}}/\text{kJ}/\text{mol}$						VEC	$r/\text{\AA}$	$T_m/\text{K}$
	Ta	Nb	Zr	Ti	Fe	Cr			
Ta	−	0	3	1	−15	−7	5	1.43	3290
Nb	−	−	4	2	−16	−7	5	1.43	2750
Zr	−	−	−	0	−25	−12	4	1.6	2128
Ti	−	−	−	−	−17	−7	4	1.46	1941
Fe	−	−	−	−	−	−1	8	1.24	1811
Cr	−	−	−	−	−	−	6	1.25	2182

Solution strengthening is expressed as:

$$\sigma_s = \left( \sum A^{\frac{3}{2}} G^{\frac{3}{2}} c_i f_i^2 \right)^{\frac{2}{3}} \tag{9}$$

where  $A$  is a constant,  $A = 0.04$  [23];  $G$  is the shear modulus,  $G = \sum c_i G_i$ ;  $f_i$  is expressed as:

$$f_i = \sqrt{\alpha^2 \delta_{r_i}^2 + \delta_{G_i}^2} \tag{10}$$

where  $\alpha$  is determined by the dislocation type constant,  $\alpha = 9$  [34];  $\delta_{r_i}$  and  $\delta_{G_i}$  is atomic mismatch and modulus mismatch, expressed as:

$$\delta_{r_i} = \frac{9}{8} \sum c_j \frac{2(r_i - r_j)}{r_i + r_j} \tag{11}$$

$$\delta_{G_i} = \frac{9}{8} \sum c_j \frac{2(G_i - G_j)}{G_i + G_j} \tag{12}$$

TaNbZrTi is a double BCC structure,  $\sigma_s = \psi_1 \sigma_{s1} + \psi_2 \sigma_{s2}$ ,  $\sigma_{s1}$  and  $\sigma_{s2}$  corresponding BCC1 and BCC2 phase of solid solution strengthening,  $\psi_1$  and  $\psi_2$  corresponds to the volume fraction of them [35]. BCC1 phase of solid solution strengthening  $\sigma_{s1} = 740.5$  MPa, solid solution strengthening of BCC2 phase  $\sigma_{s2} = 777.1$  MPa, total solid solution strengthening contribution was 747.5 MPa.

With Fe<sub>2</sub>Nb precipitation strengthening phase in the coating, precipitation strengthening  $\sigma_p$  contribution could not be ignored.  $\sigma_p$  can be divided into coherent strengthen ( $\sigma_{cs}$ ), modulus of strengthening ( $\sigma_{ms}$ ) and orderly strengthening ( $\sigma_{os}$ ) [36]:

$$\sigma_{cs} = M \alpha_\epsilon \left( G_p \epsilon_c \right)^{\frac{3}{2}} \left( \frac{r_p f_p}{0.5 G_p b} \right)^{\frac{1}{2}} \tag{13}$$

$$\sigma_{ms} = 0.0055 M (\Delta G)^{\frac{3}{2}} \left( \frac{2 f_p}{G_p} \right)^{\frac{1}{2}} \left( \frac{r_p}{b} \right)^{\frac{3m}{2} - 1} \tag{14}$$

$$\sigma_{os} = 0.81 M \frac{\gamma_p}{2b} \left( \frac{3\pi f_p}{8} \right)^{\frac{1}{2}} \tag{15}$$

where  $M$  is the Taylor factor,  $M = 2.73$  [37];  $r_p$  and  $f_p$  are the average radius and volume fraction of precipitation, which are 186 nm, and 2.3%, respectively;

$\alpha_\epsilon$  is constant,  $\alpha_\epsilon = 2.6$ ;  $\epsilon_c$  is constraint lattice mismatch strain,  $\epsilon_c = \frac{2}{3} \epsilon = 0.003$ ;  $b$  is the Burgers vector,  $b = \frac{\sqrt{2}}{2} a = 0.233$  nm,  $a$  is the lattice constant;  $m$  is a constant,  $m = 0.85$ ;  $\Delta G$  is the shear modulus difference between the precipitated particles and the alloy;  $G_p$  is the shear modulus of precipitated particles, and the shear modulus of Fe<sub>2</sub>Nb is 91.8 GPa [38].  $\gamma_p$  is precipitation antiphase-boundary energy,  $\gamma_p = 0.2$  J/m<sup>2</sup> [36, 39].

According to Eq. (13), (14) and (15), and calculated the  $\sigma_{cs} = 648.8$  MPa,  $\sigma_{ms} = 57.7$  MPa,  $\sigma_{os} = 44.6$  Mpa,  $\sigma_p = \sigma_{cs} + \sigma_{ms} + \sigma_{os} = 751.1$  Mpa. Figure 14 shows the calculated yield strength of A-HEA (this work), T-HEA and As-HEA (As-HEA) [26]. Yield strength of T-HEA was 1051.1 MPa, which was consistent with the yield strength of as-cast TaNbZrTi RHEA (1100 ± 90 MPa) [26]. It has been reported that the yield strength of RHEAs is about 3 times that of Vickers hardness [23]. The theoretical yield strength of A-HEA was 1816.1 MPa, which was basically in line with practice. The contribution of solid solution strengthening, precipitation strengthening, fine crystal strengthening and alloy foundation strength to yield strength was 41.1%, 41.5%, 5.5%, and 11.9%, respectively. The high yield strength of the alloy was mainly due to solid solution strengthening and Fe<sub>2</sub>Nb precipitation strengthening.

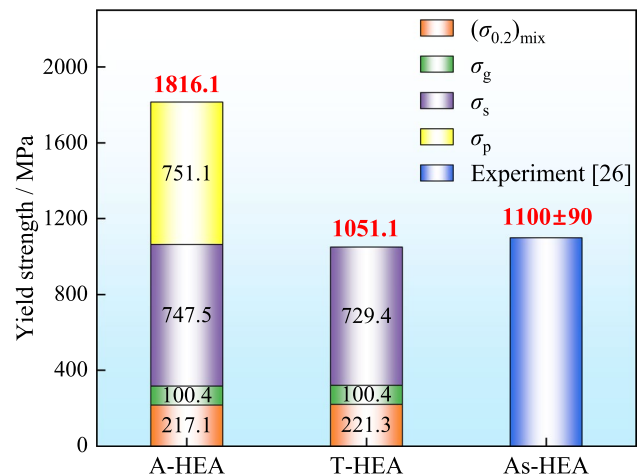


**Figure 14** Yield strength of A-HEA (this work), T-HEA and As-HEA. The experimental yield strength of As-HEA is derived from [26].

### High-temperature oxidation mechanism

The following results were obtained from the high-temperature oxidation experiment:

- The oxidation resistance of BCC1 phase was better than that of BCC2 phase.
- O element was mainly propagated internally by BCC2.
- Cracks appeared in BCC2 oxide film.
- Oxide film had protective effect at 800 and 1000 °C, but it was failure at 1200 °C, resulting in serious internal oxidation of the coating.

Based on the aforementioned results, a comprehensive analysis of the high-temperature oxidation mechanism can be elucidated. Primarily, the BCC2 phase, characterized by its rich Zr and Ti content, underwent a transformation from BCC structure to HCP structure above the temperature threshold of 800 °C [35, 40]. It is important to note that these distinct phases possess varying atomic packing densities, with BCC, FCC, and HCP phases having densities of 68%, 74%, and 74%, respectively [6]. Consequently, HCP phase occupies a smaller volume compared to BCC phase while containing the same number of atoms. This phase transition results in a volume shrinkage within BCC2 phase, accompanied by phase transition stress. Notably, this transition disrupts the bond between the BCC1 and BCC2

phases, creating a pathway for the facilitated diffusion of O inward along BCC2 phase. Concurrently, the volume shrinkage exerts greater constraint stress on the oxide layer attached to BCC2 phase, ultimately leading to its rupture. Furthermore, it is essential to consider the thermodynamic aspects of the structural transition. BCC structures generally exhibit lower total energy levels, signifying superior thermodynamic stability [6]. Following the transformation to HCP structure, the BCC2 phase becomes more susceptible to oxidation, further exacerbating the oxidation process.

Figure 15 presents a schematic diagram of the high-temperature oxidation mechanism, highlighting the significance of the protective effect of the oxide layer in determining the high-temperature oxidation resistance of the coating. The oxide layer was mainly composed of TiO<sub>2</sub>, Nb<sub>2</sub>O<sub>5</sub>, and Fe<sub>2</sub>O<sub>3</sub>, and its oxidation reaction was [41]:



Whether dense oxide layer can be formed is calculated according to the Pilling–Bedworth ratio (PBR). PBR of 1–2 indicates that the oxide layer has protective effect. PBR is expressed as [41]:

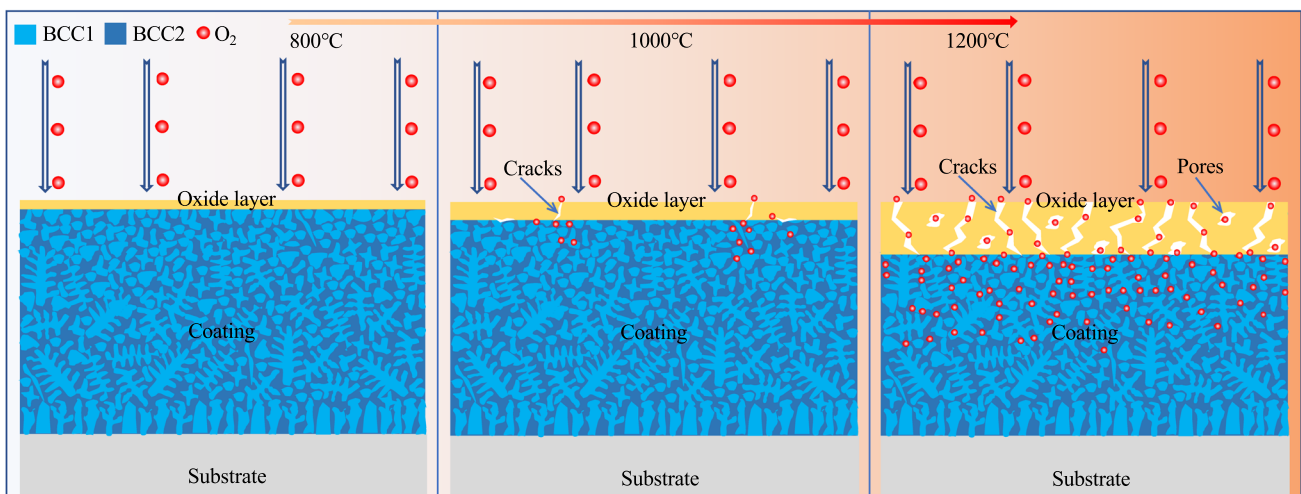


**Figure 15** Schematic diagram of high-temperature oxidation mechanism.



$$\text{PBR} = \frac{M_{\text{O}}\rho_{\text{A}}}{n_{\text{AO}}M_{\text{A}}\rho_{\text{O}}} \quad (19)$$

where  $M_{\text{O}}$  and  $M_{\text{A}}$  are the molar mass of oxide molecule and metal atom;  $\rho_{\text{O}}$  and  $\rho_{\text{A}}$  are the density of oxide and metal;  $n_{\text{AO}}$  is the number of metal atoms in an oxide molecule.

TiO<sub>2</sub>, Nb<sub>2</sub>O<sub>5</sub> and Fe<sub>2</sub>O<sub>3</sub> exhibited PBR values of 1.8, 2.74, and 2.14, respectively, as calculated using Eq. (19). Consequently, Nb<sub>2</sub>O<sub>5</sub> and Fe<sub>2</sub>O<sub>3</sub> did not provide a protective effect, and the oxidation reactions became more facile with increasing temperature. The elevated content of Nb<sub>2</sub>O<sub>5</sub> and Fe<sub>2</sub>O<sub>3</sub> contributed to heightened internal stress within the mixed oxide layer, resulting in the fracture of the oxide film and subsequent catastrophic oxidation. On one hand, the diffusion of substrate elements led to the formation of the Fe<sub>2</sub>Nb precipitate phase, thereby enhancing the coating strength. On the other hand, Fe diffusion had an adverse effect on the coating oxidation resistance at high temperatures. This dual effect underscores the intricate factors influencing the high-temperature oxidation behavior of the coating.

## Conclusion

In this study, the appropriate process parameters were determined through a series of single-channel LC experiments. Subsequently, a TaNbZrTi RHEA coating was fabricated by LC, and the microstructure and strengthening mechanism of the coating were analyzed. Finally, the high-temperature oxidation behavior of the coating in the temperature range of 800 to 1200 °C was discussed, along with an analysis of the high-temperature oxidation mechanism. The conclusion is described as follows:

1. The coating is composed of the primary BCC1 phase, rich in Ta and Nb, the secondary BCC2 phase, rich in Zr and Ti, and the intermetallic compound Fe<sub>2</sub>Nb. The top layer of the coating exhibits a fine cellular crystal morphology (with a size of 5.71 μm), while the central region displays gross dendrites, and the overlapping area features plate strip grains.
2. The theoretical yield strength of the coating is calculated to be 1816.1 MPa. The contributions to yield strength from solid solution strengthening, precipitation strengthening, fine crystal strengthening, and alloy foundation strength are estimated to be 41.1%, 41.5%, 5.5%, and 11.9%, respectively. Notably, the Fe<sub>2</sub>Nb phase, formed as a result of substrate element diffusion, demonstrates significant precipitation strengthening effects, contributing to the overall enhancement of the coating strength.
3. At temperatures of 800, 1000, and 1200 °C, the oxide layer thickness on the coating measures 1.4, 2.9, and 34.5 μm, respectively. During high-temperature exposure, the BCC2 phase undergoes a transition from BCC to HCP, resulting in reduced thermal stability and the development of phase transition stress, ultimately leading to the fracture of the oxide layer. Additionally, the diffusion of Fe elements increases the PBR of the oxide layer, causing a loss of protective effectiveness at 1200 °C and resulting in catastrophic oxidation.

## Data and code availability

Not applicable.

## Acknowledgements

This work was supported by the National Key Research and Development Program (2023YFE0201600), the Fundamental Research Funds for the Central Universities (2021ZDPY0223), and a Project Funded by the Priority Academic Program Development of Jiangsu Higher Education Institutions.

## Author contribution

JLZ: Writing—original draft, Methodology, Investigation, Formal analysis. YHC: Methodology, Data curation, Validation, Writing—review & editing. HC: Data curation, Visualization. KM: Resources. YXW: Investigation, Resources. JYY: Writing—review & editing.

## Declarations

**Conflict of interest** The authors declare that they have no known competing financial interests or personal relationships that could have appeared to influence the work reported in this paper.

**Ethical approval** Not applicable.

## References

- [1] Liu H, Yang D, Jiang Qi, Jiang Y, Yang W, Liu L, Zhang L-C (2023) Additive manufacturing of metallic glasses and high-entropy alloys: significance, unsettled issues, and future directions. *J Mater Sci Technol* 140:79–120
- [2] Tang Y, Wang R, Xiao B, Zhang Z, Li S, Qiao J, Bai S, Zhang Y, Liaw PK (2023) A review on the dynamic-mechanical behaviors of high-entropy alloys. *Progress Mater Sci* 8:101090
- [3] Kloenne ZT, Couzinié JP, Heczko M, Gröger R, Viswanathan GB, Clark WAT, Fraser HL (2023) On the bcc/B2 interface structure in a refractory high entropy alloy. *Scripta Mater* 223:115071
- [4] Liu C-J, Gadelmeier C, Shao-Lun Lu, Yeh J-W, Yen H-W, Gorsse S, Glatzel U, Yeh A-C (2022) Tensile creep behavior of HfNbTaTiZr refractory high entropy alloy at elevated temperatures. *Acta Mater* 237:118188
- [5] Li W, Xiong K, Yang L, Zhang S, He J, Wang Y, Mao Y (2022) An ambient ductile TiHfVNbTa refractory high-entropy alloy: cold rolling, mechanical properties, lattice distortion, and first-principles prediction. *Mater Sci Eng A* 856:144046
- [6] Zhou J-l, Cheng Y-H, Chen Y-X, Liang X-B (2022) Composition design and preparation process of refractory high-entropy alloys: a review. *Int J Refract Metal Hard Mater* 105:105836
- [7] Zhang X, Cui X, Jin G, Ding Q, Zhang D, Wen X, Jiang L, Wan S, Tian H (2022) Microstructure evolution and properties of NiTiCrNbTa<sub>x</sub> refractory high-entropy alloy coatings with variable Ta content. *J Alloys Compd* 891:161756
- [8] Deng J, Yang J, Lv L, Zhang W, Chen Q, Zhou M, Zhu C, Liu N, Yang J (2022) Corrosion behavior of refractory TiNbZrMoV high-entropy alloy coating in static lead-bismuth eutectic alloy: a novel design strategy of LBE corrosion-resistant coating? *Surf Coat Technol* 448:128884
- [9] Tao Yu, Wang H, Han Ke, Yifan Wang Yu, Qiu BZ (2022) Mo<sub>20</sub>Nb<sub>20</sub>Co<sub>20</sub>Cr<sub>20</sub>(Ti<sub>8</sub>Al<sub>8</sub>Si<sub>4</sub>) refractory high-entropy alloy coatings fabricated by electron beam cladding: microstructure and wear resistance. *Intermetallics* 149:107669
- [10] Kuczyk M, Krülle T, Zawischa M, Kaspar J, Zimmer O, Leonhardt M, Leyens C, Zimmermann M (2022) Microstructure and mechanical properties of high entropy alloy nitride coatings deposited via direct current cathodic vacuum arc deposition. *Surf Coat Technol* 448:128916
- [11] Zhang W, Chabok A, Kooi BJ, Pei Y (2022) Additive manufactured high entropy alloys: a review of the microstructure and properties. *Mater Des* 220:110875
- [12] Bharat N, Bose PSC (2021) An overview on machinability of hard to cut materials using laser assisted machining. *Mater Today Proc* 43:665–672
- [13] Ouyang D, Chen ZJ, Yu HB, Chan KC, Liu L (2022) Oxidation behavior of the Ti<sub>38</sub>V<sub>15</sub>Nb<sub>23</sub>Hf<sub>24</sub> refractory high-entropy alloy at elevated temperatures. *Corros Sci* 198:110153
- [14] Yan Y, McGarrity KA, Delia DJ, Fekety C, Wang K (2022) The oxidation-resistance mechanism of WTaNbTiAl refractory high entropy alloy. *Corros Sci* 204:110377
- [15] Zhang P, Li Y, Chen Z, Zhang J, Shen B (2019) Oxidation response of a vacuum arc melted NbZrTiCrAl refractory high entropy alloy at 800–1200 °C. *Vacuum* 162:20–27
- [16] Wang Q, Kong X, Xiaoyong Wu, Lu Wu, You Yu, Xin T, Qin J (2022) Effect of the local chemical environment on oxidation resistance mechanisms in AlNbTiZr refractory high entropy alloys: a first-principles study. *Scripta Mater* 213:114624
- [17] Yurchenko N, Panina E, Zherebtsov S, Stepanov N (2022) Oxidation behaviour of eutectic refractory high-entropy alloys at 800–1000 °C. *Corros Sci* 205:110464
- [18] Yi G, Ding Yi, Cheng Y, Zhang P, Wang X, Liang X (2022) Development and oxidation behavior of high entropy silicide (NbMoTaWV)Si<sub>2</sub> coatings on NbMoTaWV alloy. *J Alloys Compd* 916:165384
- [19] Schellert S, Gorr B, Laube S, Kauffmann A, Heilmaier M, Christ HJ (2021) Oxidation mechanism of refractory high entropy alloys Ta–Mo–Cr–Ti–Al with varying Ta content. *Corros Sci* 192:109861
- [20] Qiao D, Liang H, Shiyu W, He J, Cao Z, Yiping L, Li T (2021) The mechanical and oxidation properties of novel B2-ordered Ti<sub>2</sub>ZrHf<sub>0.5</sub>VNb<sub>0.5</sub>Al<sub>x</sub> refractory high-entropy alloys. *Mater Charact* 178:111287
- [21] Lou LY, Liu KC, Jia YJ, Ji G, Wang W, Li CJ, Li CX (2022) Microstructure and properties of lightweight Al<sub>0.2</sub>CrNbTiV refractory high entropy alloy coating with different dilutions deposited by high speed laser cladding. *Surf Coat Technol* 447:128873
- [22] Rasiya G, Shukla A, Saran K (2021) Additive manufacturing—a review. *Mater Today Proc* 47(19):6896–6901
- [23] Ji G, Zhou Z, Meng F, Yang X, Sheng R, Qiao J, Liaw PK, Li Mo, Jiang L, Chen S, Tong Y (2022) Effect of Zr addition on the local structure and mechanical properties of Ti–Ta–Nb–Zr refractory high-entropy alloys. *J Market Res* 19:4428–4438
- [24] Zhou J-l, Yang J-Y, Zhang X-F, Ma F-W, Ma K, Cheng Y-H (2023) Research status of tribological properties

- optimization of high-entropy alloys: a review. *J Mater Sci* 58:4257–4291
- [25] Xiang T, Zhao M, Peng Du, Xie G (2023) Heat treatment effects on microstructure and mechanical properties of TiZrNbTa high-entropy alloy. *J Alloys Compd* 930:167408
- [26] Nguyen VT, Qian M, Shi Z, Song T, Huang L, Zou J (2018) A novel quaternary equiatomic Ti–Zr–Nb–Ta medium entropy alloy (MEA). *Intermetallics* 101:39–43
- [27] Zhou JL, Cheng YH, Yang JY, Wang QQ, Liang XB (2021) Effects of WS<sub>2</sub> and Ti<sub>3</sub>AlC<sub>2</sub> additions on the high temperature wear properties of laser cladding YW1/NiCoCrAlY tool coating. *Ceram Int* 47(24):35124–35133
- [28] Zhou J, Kong D (2020) Immersion corrosion and electrochemical performances of laser clad FeSiB, FeSiBCr and FeSiBCrMo coatings in 3.5 wt% NaCl solution. *Surface Coat Technol* 383:125229
- [29] Welch NJ, Quintana MJ, Butler TM, Collins PC (2023) High-temperature oxidation behavior of TaTiCr, Ta<sub>4</sub>Ti<sub>3</sub>Cr, Ta<sub>2</sub>TiCr, and Ta<sub>4</sub>TiCr<sub>3</sub> concentrated refractory alloys. *J Alloys Compd* 941:169000
- [30] Chen L, Yang Z, Linkai Lu, Zhang X, Ren X (2023) Effect of TiC on the high-temperature oxidation behavior of WMoTaNbV refractory high entropy alloy fabricated by selective laser melting. *Int J Refract Metal Hard Mater* 110:106027
- [31] Junhao Hu, Cang Gu, Li J, Li C, Feng J, Jiang Y (2023) Microstructure and oxidation behavior of the Y/Ta/Hf co-doped AlCoCrFeNi high-entropy alloys in air at 1100 °C. *Corros Sci* 212:110930
- [32] He H, Lai M, Liu C, Zeng G, He L, Zhang W, Yi J, Liu S, Long J (2023) Effects of deposition temperature on the microstructure, mechanical properties, high temperature corrosion and oxidation properties of AlCrNbTiZr high entropy alloy coatings. *Int J Refract Metal Hard Mater* 112:106156
- [33] Feng R, Feng B, Gao MC et al (2021) Superior high-temperature strength in a supersaturated refractory high-entropy alloy. *Adv Mater* 33(48):2102401
- [34] Juan C-C, Tsai M-H, Tsai C-W, Hsu W-L, Lin C-M, Chen S-K, Lin S-J, Yeh J-W (2016) Simultaneously increasing the strength and ductility of a refractory high-entropy alloy via grain refining. *Mater Lett* 184:200–203
- [35] Wu Z, Bei H, Pharr GM, George EP (2014) Temperature dependence of the mechanical properties of equiatomic solid solution alloys with face-centered cubic crystal structures. *Acta Mater* 81:428–441
- [36] Yuan JL, Wu YC, Liaw PK, Luan JH, Jiao ZB, Li J, Han PD, Qiao JW (2022) Remarkable cryogenic strengthening and toughening in nano-coherent CoCrFeNiTi<sub>0.2</sub> high-entropy alloys via energetically-tuning polymorphous precipitates. *Mater Sci Eng A* 842:143111
- [37] Jin D, Wang Z, Yuan J, Jiang B, Fengyun Yu, Li J, Wang Q (2023) High-strength and energetic Al<sub>2</sub>Ti<sub>6</sub>Zr<sub>2</sub>Nb<sub>3</sub>Ta<sub>3</sub> high entropy alloy containing a cuboidal BCC/B2 coherent microstructure. *J Alloys Compd* 931:167546
- [38] Qi JJ, Zhou Y, Wang W, Qian LH, Lv ZQ, Fu WT (2018) Electronic, magnetic and mechanical properties of (Fe, Ni)<sub>2</sub>Nb from density functional theory. *J Magn Magn Mater* 452:219–229
- [39] Kozar R, Suzuki A, Milligan W et al (2009) Strengthening mechanisms in polycrystalline multimodal nickel-base superalloys. *Metall Mater Trans A* 40:1588–1603
- [40] Dobbstein H, Gurevich EL, George EP, Ostendorf A, Laplanche G (2019) Laser metal deposition of compositionally graded TiZrNbTa refractory high-entropy alloys using elemental powder blends. *Addit Manuf* 25:252–262
- [41] Zhao P, Li J, Zhang Y, Li X, Xia MM, Yuan BG (2021) Wear and high-temperature oxidation resistances of AlNbTaZr<sub>x</sub> high-entropy alloys coatings fabricated on Ti6Al4V by laser cladding. *J Alloys Compd* 862:158405

**Publisher's Note** Springer Nature remains neutral with regard to jurisdictional claims in published maps and institutional affiliations.

Springer Nature or its licensor (e.g. a society or other partner) holds exclusive rights to this article under a publishing agreement with the author(s) or other rightsholder(s); author self-archiving of the accepted manuscript version of this article is solely governed by the terms of such publishing agreement and applicable law.